

A Fisher-Rao metric for paracatadioptric images of lines

16th September 2011

Stephen J. Maybank¹, Siohoi Ieng² and Ryad Benosman²

Abstract. In a central paracatadioptric imaging system a perspective camera takes an image of a scene reflected in a paraboloidal mirror. A 360° field of view is obtained, but the image is severely distorted. In particular, straight lines in the scene project to circles in the image. These distortions make it difficult to detect projected lines using standard image processing algorithms.

The distortions are removed using a Fisher-Rao metric which is defined on the space of projected lines in the paracatadioptric image. The space of projected lines is divided into subsets such that on each subset the Fisher-Rao metric is closely approximated by the Euclidean metric. Each subset is sampled at the vertices of a square grid and values are assigned to the sampled points using an adaptation of the trace transform. The result is a set of digital images to which standard image processing algorithms can be applied. The effectiveness of this approach to line detection is illustrated using two algorithms, both of which are based on the Sobel edge operator. The task of line detection is reduced to the task of finding isolated peaks in a Sobel image. An experimental comparison is made between these two algorithms and third algorithm taken from the literature and based on the Hough transform.

Keywords: central projection, Fisher-Rao metric, Hough transform, line detection, paraboloidal mirror, paracatadioptric system, Sobel operator, trace transform.

1 Introduction

A catadioptric imaging system consists of a perspective pin hole camera and a mirror, such that the camera takes an image of the scene reflected in the mirror. If the mirror is curved appropriately, and if the camera is correctly placed in relation to the mirror, then the resulting image has a very wide field of view. This property has led to the extensive use of catadioptric systems in visual surveillance. A few catadioptric imaging systems can together survey an area that would otherwise require a much larger number of conventional perspective cameras (Baker and Nayar 1999).

In a central paracatadioptric imaging system the mirror has the shape of a paraboloid and the optical axis of the camera is parallel to the axis of the mirror, as shown in Fig. 1. This system has two advantages. Firstly, all the rays that enter the perspective camera are reflections of rays that were originally directed towards a single point in space, namely the focal point F of the mirror. Secondly, the construction of a central paracatadioptric imaging system is simpler than the construction of other types of central catadioptric imaging systems (Baker and Nayar 1999). This is because in a central paracatadioptric

¹Department of Computer Science and Information Systems, Birkbeck College, Malet Street, London, WC1E 7HX, UK.

²Institut des Systèmes Intelligents et de Robotique, Université Pierre et Marie Curie, 4 Place Jussieu, CC 173, 75252, Paris Cedex 05, France.

system it is only necessary to ensure that the optical axis of the camera is parallel to the axis of the mirror and that the camera is in focus for objects at infinity. In practice the optical centre of the camera is usually placed on or near to the axis of the mirror. All the catadioptric systems discussed in this paper are central systems. For a discussion of non-central catadioptric systems see Gasparini and Caglioti (2011).

A disadvantage of catadioptric imaging systems is that the image is severely distorted (Barreto and Araujo 2001). It is necessary to take this distortion into account when searching for particular structures. For example, the straight lines in a scene project to circles in a paracatadioptric image. In order to simplify the task of detecting the projected lines, the paracatadioptric image can itself be distorted to produce a new image defined on a sphere, such that the projected lines correspond to great circles on the sphere (Bazin et al. 2007a; Vasseur and Mouaddib 2004; Ying and Hu 2004). In the spherical model for the paracatadioptric image the natural measure of distance between two great circles with unit normal vectors n_1 and n_2 is

$$\cos^{-1}(n_1 \cdot n_2),$$

however, this distance is not closely related to distances measured in the original paracatadioptric image.

In this paper the space of projected lines in a paracatadioptric image is parameterised using a small number of subsets of the Euclidean plane \mathbb{R}^2 . The distances between pairs of lines in the paracatadioptric image are measured using the Fisher-Rao metric (Amari 1985; Cover and Thomas 1991). These distances are closely related to the problem of distinguishing between two projected lines using feature points which might be sampled from either line. If the Fisher-Rao distance between the two projected lines is small, then it is difficult to distinguish between them using a small number of feature points. Conversely, if the Fisher-Rao distance between the projected lines is large, then it is easy to distinguish between them using feature points. The parameterisation of the space of projected lines by subsets of \mathbb{R}^2 can be and is chosen such that the Euclidean distance between any two points in a given subset closely approximates to the Fisher-Rao distance between the corresponding projected lines. Each of the chosen subsets of \mathbb{R}^2 is sampled at the vertices of a square grid to produce a digital image. The pixel values are obtained using an adaptation of the trace transform (Kadyrov and Petrou 2001). Once these digital images have been obtained, it is straightforward to apply algorithms developed for processing digital images to tasks such as the detection of projected lines in a paracatadioptric image. Two such algorithms, both of which are based on the Sobel operator, are described in Section 7.3. The effectiveness of this approach for detecting projected lines is apparent in the simple specifications and good performances of these two algorithms.

The construction of the subsets of \mathbb{R}^2 which are used to parameterise the space of projected lines in a paracatadioptric image involves a sequence of four Riemannian manifolds together with functions from one Riemannian manifold to the next. The points in each of the Riemannian manifolds correspond to projected lines. The first manifold in the sequence is obtained using an approximation to the Fisher-Rao metric for the projected lines in a paracatadioptric image. The last manifold is a subset of \mathbb{R}^2 with the Euclidean metric. Each function is either an exact isometry, or an isometry to within a small error. (An isometry is a diffeomorphism from one Riemannian manifold to another with the property that it preserves the distances between points.)

In order to define the Fisher-Rao metric, each projected line has associated with it a probability density function (pdf) that models a blurred version of the line. The distance between any two projected lines is defined to be the distance between the associated pdfs, as measured using the Fisher-Rao metric (Amari 1985; Cover and Thomas 1991; Maybank 2004). The square of the distance between two nearby projected lines is closely approximated by one half of the average of the log likelihood ratio of the two pdfs associated with the lines. If two projected lines are close together in the Fisher-Rao metric, then it is difficult to distinguish between them using measurements in the paracatadioptric image.

The following aspects of this work are new.

- The definition of a Fisher-Rao metric on the parameter space T for the projected lines in a paracatadioptric image.
- The division of T into a small number of subsets such that on each subset the Fisher-Rao metric is closely approximated by the Euclidean metric.
- The construction of algorithms for detecting projected lines by applying standard image processing methods to digital images equipped with the Euclidean metric. The pixels in these digital images correspond to points of T . The resulting algorithms are simple and efficient, with few parameters that have to be specified in advance or tuned.

1.1 Related work

The theory of central catadioptric cameras is described in detail by Baker and Nayar (1999). They show that a physically realisable central catadioptric system can be obtained only if the mirror is a plane, an ellipsoid, a paraboloid or a hyperboloid of two sheets. In a central catadioptric system all the rays which enter the camera are reflections of rays which were originally directed towards a single point in space. Geyer and Daniilidis (2001) show that the projection from space to an image in any central catadioptric system can be modeled geometrically using a sphere and a projection plane. The separate components of the model are not physically realistic, but when taken together they do describe the correct physical projection from space to the image plane.

Methods for detecting the projections of lines into a catadioptric image are described by Bazin et al. (2007a), Vasseur and Mouaddib (2004) and Ying and Hu (2004). In each case the catadioptric image is reparameterised such that the projected lines correspond to great circles on a sphere. Bazin et al. (2007a) chain edge elements on the sphere and then fit great circles to the chains. Vasseur and Mouaddib (2004) and Ying and Hu (2004) detect the projected lines using a two-dimensional Hough space in which the points correspond to great circles on the sphere. The application of a randomised Hough transform to the detection of great circles on spheres is described by Torii and Imiya (2007). Pinciroli et al. (2005) detect the projections of vertical and horizontal lines into a conical catadioptric image. The projections of the vertical lines are found by chaining edge elements. The projections of the horizontal lines are found using RANSAC. It is noted that a conical catadioptric system is not a central imaging system. The projections of rectangles into catadioptric images are found by Bazin et al. (2007b). Duan et al. (2010) detect ellipses in catadioptric images. These are ellipses as defined in the image.

They are not necessarily the projections of ellipses in space. A method for overcoming the effects of the distortion of catadioptric images is described by Daniilidis et al. (2002). They formulate image processing algorithms, such as filtering, on a sphere in which the great circles are projected lines. They then use the pixel values in the catadioptric image directly rather than infer new pixel values on the sphere by interpolation.

The Fisher-Rao metric is described by Amari (1985) and Cover and Thomas (1991). It is applied to the detection of image structures by Maybank (2004, 2005, 2007, 2008). See also Kanatani (1996), Section 14.4. If the noise level in the image is relatively low, then the Fisher-Rao metric can be closely approximated by a simpler metric which in some applications has a closed form.

1.2 Overview

The geometry of a paracatadioptric image is described in Section 2. In Section 3 the set of all projected lines is divided into disjoint subsets, depending on the way in which each projected line intersects the boundary of the image. In Section 4 approximations are obtained to the Fisher-Rao metric on each of the subsets defined in Section 3. In Sections 5 and 6 the subsets obtained in Section 3 are further divided to obtain the sets on which the Fisher-Rao metric is closely approximated by the Euclidean metric. Two new algorithms for detecting projected lines are described in Section 7. Both algorithms are based on the Sobel operator. The new algorithms are compared experimentally with a third algorithm based on the Hough detector. Some concluding remarks are made in Section 8. The calculations described in this paper were carried out using Mathematica, version 7.0.

2 The Paracatadioptric Image

The projection to a paracatadioptric image is described in Section 2.1. It is shown that a straight line in space which is not coplanar with the axis of the paraboloidal mirror projects to a circle in the paracatadioptric image. The principal point of the paracatadioptric image is, by definition, the point at which the axis of the mirror intersects the image plane. The intersections of a projected line with a given circle centred at the principal point are described in Section 2.2.

This section is included to establish the notation and to make the paper more self-contained. Detailed discussions of paracatadioptric and catadioptric systems can be found in Baker and Nayar (1999) and in Geyer and Daniilidis (2000).

2.1 Projection of a line

Consider a paracatadioptric camera, in which the mirror is by definition a parabolic surface. Cartesian coordinates x, y, z are chosen in \mathbb{R}^3 such that the equation of the surface is

$$4az = x^2 + y^2, \tag{1}$$

where a is a strictly positive number. The focal point of the mirror is $F = (0, 0, a)^\top$. A ray of light directed towards F and incident on the mirror as shown in Fig. 1, is reflected

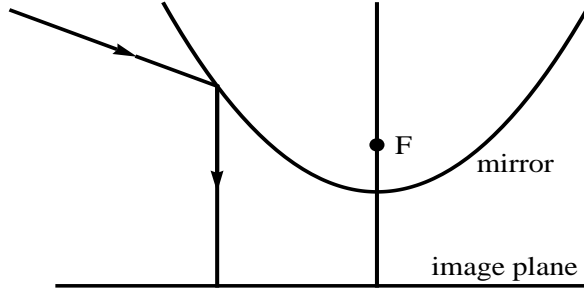


Figure 1: A paracatadioptric camera.

to produce a ray anti-parallel to the z -axis. The reflected ray is incident on an image plane parallel to the x, y plane of the chosen coordinate system. The x, y coordinates in \mathbb{R}^3 also serve as coordinates in the image plane. The axis of the mirror is the z -axis and the principal point in the image is given by $x = 0, y = 0$.

It is well known that a general straight line in space projects to a circle in a paracatadioptric image (Geyer and Daniilidis 2000). The details are summarised here for completeness. Any given line in \mathbb{R}^3 , which is not incident to F , is projected to a curve in the image plane. Let Π be the plane in \mathbb{R}^3 spanned by the line and the point F . Then Π projects to the same image curve as the line. The equation for Π is of the form

$$l_1x + l_2y + l_3(z - a) = 0, \quad (2)$$

where $(l_1, l_2, l_3)^\top$ is a unit vector. The set of such planes forms a two dimensional real projective space \mathbb{P}^2 . The plane (2) cuts the mirror in a curve which projects down to the curve in the image plane defined by

$$4al_1x + 4al_2y + l_3(x^2 + y^2 - 4a^2) = 0. \quad (3)$$

If $l_3 \neq 0$, then (3) is a circle with centre c and radius r given by

$$c = -2al_3^{-1}(l_1, l_2)^\top, \quad (4)$$

$$r = 2al_3^{-1}. \quad (5)$$

Let c_1, c_2 be the components of c . On eliminating l_1, l_2, l_3 from (4), (5), it follows that

$$r^2 = c_1^2 + c_2^2 + 4a^2. \quad (6)$$

Conversely, if (6) holds, then the circle with centre c and radius r is the projection of a plane Π which contains F and which has an equation of the form (3), with $l_3 \neq 0$. It is apparent from (6) that r can be written as a function of c , $r(c) \equiv r$.

If $l_3 = 0$, then the plane (2) contains the z -axis and the projection of the plane is a line

$$l_1x + l_2y = 0 \quad (7)$$

which contains the origin. Conversely, any image line which contains the origin is the projection of a plane of the form (2) with $l_3 = 0$.

2.2 Properties of the images of lines

Let \tilde{T} be the family of curves obtained as images of straight lines which do not contain the focal point F of the paraboloidal mirror. The family \tilde{T} contains a two parameter family of circles and the one parameter family of straight lines through the origin. Let θ be an element of \tilde{T} and let $C(\theta)$ be the set of points in the image plane on the curve defined by θ . Suppose that θ is a circle with centre c and radius r , denoted by $\theta = (c, r)$. Let $\|c\|$ be the Euclidean length of c . It follows from (6) that $r > \|c\|$, thus $C(\theta)$ bounds a disk which contains the origin. The maximum distance from the origin to a point of $C(\theta)$ is

$$r + \|c\|. \quad (8)$$

On using (6) to express r as a function of $\|c\|$, it follows that (8) is an increasing function of $\|c\|$. The minimum distance from the origin to a point of $C(\theta)$ is

$$r - \|c\|. \quad (9)$$

On using (6) to express r as a function of $\|c\|$, it follows that (9) is a decreasing function of $\|c\|$.

In many applications, the image I taken by a paracatadioptric system has the form of a disk or annulus centred at the principal point. In order to study the properties of the projections of lines into a paracatadioptric image, it is useful to describe those cases in which the projection $C(\theta)$ of a line intersects the boundary of I . Let θ be the circle $\theta = (c, r)$, let q be the function defined on $[0, \infty) \times [0, 2\pi)$ such that

$$q(\xi, \phi) = (\xi \cos(\phi), \xi \sin(\phi))^T, \quad 0 \leq \xi < \infty, 0 \leq \phi < 2\pi, \quad (10)$$

and let $\alpha \in [0, 2\pi)$ be the angle such that $q(\|c\|, \alpha) = c$. Let C be a circle centred at the origin and with radius R , such that $C(\theta) \neq C$ and $C(\theta) \cap C$ is non-empty. Let μ be the angle in the interval $[0, \pi]$ defined such that

$$\cos(\mu) = (R^2 - \|c\|^2 - r^2)/(2r\|c\|). \quad (11)$$

A short calculation shows that $C(\theta) \cap C$ consists of the points

$$c + q(r, \alpha - \mu) \quad \text{and} \quad c + q(r, \alpha + \mu),$$

as illustrated in Fig. 2.

It follows from (6), (11) and the condition $|\cos(\mu)| \leq 1$ that $C(\theta)$ intersects C if and only if

$$\|c\| \geq \frac{1}{2} |R - 4a^2 R^{-1}|. \quad (12)$$

If equality holds in (12), then $C(\theta)$ is tangent to C . There are two cases of tangency to consider, depending on whether $C(\theta)$ is inside or outside the disc bounded by C . It follows from (9) that if $C(\theta)$ is tangent to C and outside the open disk bounded by C , then $r - \|c\| = R$, which, together with (6), yields

$$\|c\| = \frac{1}{2} (4a^2 R^{-1} - R).$$

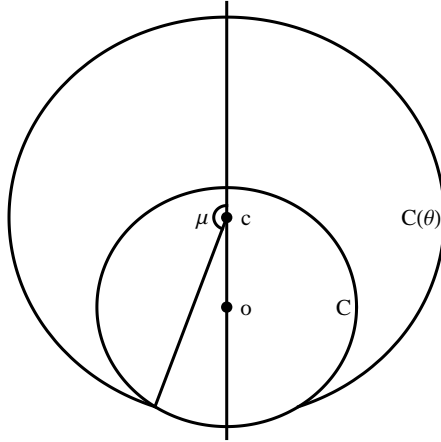


Figure 2: Intersection of the circle $C(\theta)$ with a circle C . The point c is the centre of $C(\theta)$ and o is the centre of C .

If $\|c\|$ is decreased slightly, then the minimum distance $r - \|c\|$ from $C(\theta)$ to the origin increases slightly and $C(\theta)$ ceases to intersect C . It follows that the whole of $C(\theta)$ is outside the closed disk bounded by C if and only if

$$\|c\| < \frac{1}{2} (4a^2 R^{-1} - R). \quad (13)$$

If $C(\theta)$ is tangent to C and inside the closed disk bounded by C , then it follows from (8) that $r + \|c\| = R$, which, together with (6), yields

$$\|c\| = \frac{1}{2} (R - 4a^2 R^{-1}).$$

If $\|c\|$ is decreased slightly, then the maximum distance $r + \|c\|$ from $C(\theta)$ to the origin decreases slightly and $C(\theta)$ ceases to intersect C . It follows that $C(\theta)$ is inside the closed disk bounded by C if and only if

$$\|c\| < \frac{1}{2} (R - 4a^2 R^{-1}). \quad (14)$$

3 Classification of Images of Lines

It is assumed that the image I formed by a paracatadioptric system is in the shape of an annulus, centred at the principal point. The images of lines are classified in Section 3.1 according to the way in which they intersect or fail to intersect the two circles which form the boundary of I . The parameterisations of the arcs formed by those parts of the projected images of lines contained in I are described in Section 3.2.

These results are used in Section 4 to define a Fisher-Rao metric on each class of projected lines.

3.1 Parameter space for images of lines

Let C_1, C_2 be the two concentric circles that together form the boundary of I and let R_i be the radius of C_i for $i = 1, 2$. The circles C_i are labelled such that $R_1 < R_2$. It is

convenient to include the boundary $C_1 \cup C_2$ in I , to ensure that I is a closed subset of the image plane.

As in Section 2.2, let \tilde{T} be the family of curves obtained as images of straight lines that do not contain the focal point of the paraboloidal mirror. Let T be the set of elements θ of \tilde{T} such that the corresponding curves $C(\theta)$ intersect I . Four subsets T_i , $0 \leq i \leq 3$, of T are defined as follows. An element θ of T is in T_0 if $C(\theta)$ is contained in I . The element θ is in T_1 if $C(\theta)$ intersects C_1 but does not intersect C_2 . The element θ is in T_2 if $C(\theta)$ intersects C_2 but does not intersect C_1 . Finally, θ is in T_3 if $C(\theta)$ is a circle which intersects both C_1 and C_2 .

Let $\theta = (c, r)$ be an element of T such that θ is a circle with centre c and radius r , as given by (6). It follows from the above definitions of the sets T_i , $0 \leq i \leq 3$, and from (8), (9) that

$$\begin{aligned} T_0 &= \{(c, r), r - \|c\| \geq R_1 \text{ and } r + \|c\| \leq R_2\}, \\ T_1 &= \{(c, r), r - \|c\| \leq R_1 \text{ and } r + \|c\| < R_2\}, \\ T_2 &= \{(c, r), r - \|c\| > R_1 \text{ and } r + \|c\| \geq R_2\}, \\ T_3 &= \{(c, r), r - \|c\| \leq R_1 \text{ and } r + \|c\| \geq R_2\}. \end{aligned}$$

Let $\text{int}(T_i)$ be the interior of the set T_i in \tilde{T} for $0 \leq i \leq 3$. By definition, $\text{int}(T_i)$ is the largest open set of \tilde{T} contained in T_i . It follows from the above expressions for the T_i and from (12), (13) and (14) that

$$\text{int}(T_0) = \{(c, r), \|c\| < 2^{-1}(4a^2R_1^{-1} - R_1) \text{ and } \|c\| < 2^{-1}(R_2 - 4a^2R_2^{-1})\}, \quad (15)$$

$$\text{int}(T_1) = \{(c, r), \|c\| > 2^{-1}|4a^2R_1^{-1} - R_1| \text{ and } \|c\| < 2^{-1}(R_2 - 4a^2R_2^{-1})\}, \quad (16)$$

$$\text{int}(T_2) = \{(c, r), \|c\| < 2^{-1}(4a^2R_1^{-1} - R_1) \text{ and } \|c\| > 2^{-1}|R_2 - 4a^2R_2^{-1}|\}, \quad (17)$$

$$\text{int}(T_3) = \{(c, r), \|c\| > 2^{-1}|4a^2R_1^{-1} - R_1| \text{ and } \|c\| > 2^{-1}|R_2 - 4a^2R_2^{-1}|\}. \quad (18)$$

If $R_1 = 0$, then $\text{int}(T_1)$ and $\text{int}(T_3)$ are empty. It follows from (15), (16), (17) and (18) that

- i) the sets $\text{int}(T_i)$ for $0 \leq i \leq 3$, are pairwise disjoint,
- ii) the set $\text{int}(T_0)$ is non-empty if and only if $R_1 < 2a$ and $R_2 > 2a$,
- iii) at least one of the sets $\text{int}(T_1)$, $\text{int}(T_2)$ is empty,
- iv) if $R_1 \neq 0$, then $\text{int}(T_3)$ is never empty.

Examples of elements of T_0 , T_1 and T_3 are shown in Fig. 3.

It is convenient to identify each set $\text{int}(T_i)$ with the subset of the plane defined by the centres c of the circles in $\text{int}(T_i)$. There are elements of T not contained in any of the sets $\text{int}(T_i)$, for example the lines through the common centre of the circles C_1 and C_2 . However, the set

$$T \setminus \bigcup_{i=0}^3 \text{int}(T_i)$$

has measure 0 as a subset of the two dimensional space T . For this reason it can be and is discarded without significant loss.

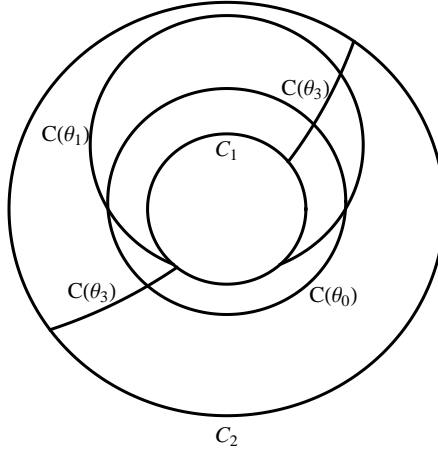


Figure 3: Examples of projected lines. The paracatadioptric image is an annulus with inner boundary C_1 and outer boundary C_2 . The circles $C(\theta_0)$, $C(\theta_1)$ and $C(\theta_3)$ are projected lines. The parameters for the paracatadioptric image in pixel units are $a = 75$, $R_1 = 100$, $R_2 = 275$.

3.2 Parameterisations of arcs in the image

For θ in $\text{int}(T_i)$, let $\Gamma(\theta)$ be that part of the circle $C(\theta)$ contained in I , $\Gamma(\theta) = C(\theta) \cap I$. If θ is in $\text{int}(T_0)$, then $\Gamma(\theta) = C(\theta)$. If θ is in $\text{int}(T_1)$, then let μ be the angle in $[0, \pi]$ such that (11) holds with $R = R_1$. The set $C(\theta) \cap C_1$ consists of the two points

$$c + q(r, \alpha - \mu) \quad \text{and} \quad c + q(r, \alpha + \mu),$$

where the function q is defined by (10) and α is the polar angle of c . The set $\Gamma(\theta)$ consists of a single arc outside the open disk bounded by C_1 and parameterised by

$$\beta \mapsto c + q(r, \beta), \quad \alpha - \mu \leq \beta \leq \alpha + \mu. \quad (19)$$

The arrow \mapsto in (19) is the usual symbol for "mapsto". If θ is in $\text{int}(T_2)$, then let μ be the angle in $[0, \pi]$ such that (11) holds with $R = R_2$. The set $\Gamma(\theta)$ consists of a single arc inside the disk bounded by C_2 and parameterised by

$$\beta \mapsto c + q(r, \beta), \quad \alpha + \mu \leq \beta \leq \alpha + 2\pi - \mu. \quad (20)$$

If θ is in $\text{int}(T_3)$, then the set $\Gamma(\theta)$ consists of two arcs. Each arc has one end point in C_1 and the other end point in C_2 . Let μ_1, μ_2 be the angles such that (11) holds with $R = R_1$ and $R = R_2$ respectively. It is noted that $\mu_1 > \mu_2$. The two arcs in $\Gamma(\theta)$ are parameterised respectively by

$$\beta \mapsto c + q(r, \beta), \quad \alpha - \mu_1 \leq \beta \leq \alpha - \mu_2, \quad (21)$$

$$\beta \mapsto c + q(r, \beta), \quad \alpha + \mu_2 \leq \beta \leq \alpha + \mu_1. \quad (22)$$

Some examples of projected lines are shown in Fig. 3. The circles C_1 and C_2 together form the boundary of a paracatadioptric image. The parameter vectors θ_0, θ_1 and θ_3 are in T_0, T_1 and T_3 respectively. Only the parts of the circles $C(\theta_1)$ and $C(\theta_3)$ within the paracatadioptric image are shown. There is no circle $C(\theta_2)$ because with the choice of parameter values specified in the caption to the Fig. 3, the set T_2 is empty.

4 Fisher-Rao Metric for Images of Lines

A Fisher-Rao metric is obtained for each of the manifolds $\text{int}(T_i)$, $0 \leq i \leq 3$ defined in Section 3.1. The advantage of the Fisher-Rao metric over other metrics on these parameter manifolds is that it is closely linked to a probabilistic description of the errors in locating points in the image.

The Fisher-Rao metric is obtained from a family of conditional probability density functions $p(x|c)$, where x is a point in the image I and c defines an element $\theta = (c, r(c))$ of $\text{int}(T_i)$. The pdf $p(x|c)$ defines a blurred version of the projected line $C(\theta(c, r(c)))$, such that $p(x|c)$ is uniform along the projected line and accurately approximated by a Gaussian along each normal to the projected line. If the Fisher-Rao distance between two pdfs $p(x|c)$ and $p(x|c')$ is small, then the blurred projected lines corresponding to c and c' are difficult to separate, given a single measurement x . If $p(x|c)$ is concentrated near to the curve $C(\theta(c, r(c)))$, then the Fisher-Rao metric has an accurate tractable approximation (Maybank 2004).

The family of conditional pdfs and the Fisher-Rao metric are defined in Section 4.1. In Section 4.2, the approximation to the Fisher-Rao metric is described and expressions for the approximating metric are obtained for each of the sets $\text{int}(T_i)$ for $0 \leq i \leq 3$. The continuity of the Fisher-Rao metric across the boundaries between the sets $\text{int}(T_i)$ is discussed in Section 4.3.

4.1 Conditional density for a measurement

It is assumed that the measurements x are points in the catadioptric image I . Let $\Gamma(\theta) = C(\theta) \cap I$ for $\theta \in T$, let $l(\Gamma(\theta))$ be the length of $\Gamma(\theta)$, as measured using the Euclidean metric in I , and let $w(x, \theta) \equiv w(x, c)$ be the signed distance from $x \in I$ to the circle $C(\theta)$ in the image plane. If $C(\theta)$ has centre c and radius r , then

$$w(x, c)^2 = (\|x - c\| - r(c))^2. \quad (23)$$

Let the unknown true value of the measurement x be a point y on $C(\theta)$. The error $x - y$ in x is modeled by the Gaussian distribution $\mathcal{N}(0, \sigma^2 I(2))$ with expected value 0, where $I(2)$ is the 2×2 identity matrix and $\sigma^2 I(2)$ is the covariance of the distribution. It is assumed that y is uniformly distributed in $\Gamma(\theta)$.

On ignoring the small effects which arise when x is near to an end point of $\Gamma(\theta)$, the conditional pdf $p(x|c)$ is given by

$$p(x|c) = l(\Gamma(\theta))^{-1} (2\pi\sigma^2)^{-1/2} \exp\left(-\frac{1}{2\sigma^2} w(x, c)^2\right), \quad x \in I. \quad (24)$$

The Fisher-Rao metric on each set $\text{int}(T_i)$ is specified by the following family of 2×2 matrices $J(c)$,

$$J_{jk}(c) = - \int_I \left(\frac{\partial^2}{\partial c_j \partial c_k} \ln p(x|c) \right) p(x|c) dx, \quad 1 \leq j, k \leq 2, c \in \text{int}(T_i).$$

For further information see Amari (1985) and Cover and Thomas (1991).

4.2 An approximation to the Fisher-Rao metric

Let s be an arc length parameter on $\Gamma(\theta)$, let $x(s)$ be the point on $\Gamma(\theta)$ corresponding to s and let $M(s)$ be the 2×2 matrix defined by

$$M_{jk}(s) = \frac{\partial^2 w(x, c)^2}{\partial c_j \partial c_k} \Big|_{x=x(s)}, \quad 1 \leq j, k \leq 2. \quad (25)$$

It is shown in Maybank (2004) that the Fisher-Rao metric $J(c)$ is approximated by the 2×2 matrix $\tilde{K}(c)$ defined by

$$\tilde{K}_{jk}(c) = \frac{1}{2\sigma^2 l(\Gamma(\theta))} \int_{\Gamma(\theta)} M_{jk}(s) ds, \quad 1 \leq j, k \leq 2. \quad (26)$$

See also Kanatani (1996), Section 14.4. Let $x(s) = (x_1(s), x_2(s))^\top$. On evaluating the derivatives in (25), the following expressions for the components $M_{jk}(s)$ of $M(s)$ are obtained,

$$M_{11}(s) = 2r(c)^{-2} x_1(s)^2, \quad (27)$$

$$M_{12}(s) = M_{21}(s) = 2r(c)^{-2} x_1(s)x_2(s), \quad (28)$$

$$M_{22}(s) = 2r(c)^{-2} x_2(s)^2. \quad (29)$$

The coordinates (c_1, c_2) are transformed to the polar coordinates (ξ, α) . The advantage in using polar coordinates is that the matrix $K(\xi, \alpha)$, which describes the approximation to the Fisher-Rao metric in the coordinate system (ξ, α) , is diagonal and independent of α . In more detail, let H be the Jacobian matrix for the coordinate transformation $(c_1, c_2) \mapsto (\xi, \alpha)$ where ξ, α are defined such that

$$(c_1, c_2)^\top = (\xi \cos(\alpha), \xi \sin(\alpha))^\top \equiv q(\xi, \alpha),$$

The matrix H is given by

$$H = \begin{pmatrix} \partial c_1 / \partial \xi & \partial c_1 / \partial \alpha \\ \partial c_2 / \partial \xi & \partial c_2 / \partial \alpha \end{pmatrix}.$$

It follows from (26) that the Fisher-Rao metric in the parameterisation (ξ, α) of $\text{int}(T_i)$ is approximated by the 2×2 matrix $K(\xi, \alpha)$ defined by

$$K(\xi, \alpha) \equiv H^\top \tilde{K}(c(\xi, \alpha)) H = \frac{1}{2\sigma^2 l(\Gamma(\theta))} \int_{\Gamma(\theta)} H^\top M(s) H ds, \quad q(\xi, \alpha) \in \text{int}(T_i). \quad (30)$$

In order to evaluate the integral on the right hand side of (30), the arc length parameter s is replaced by $r(c)\beta$, where β is an angle parameter for the arc in question. It is convenient to replace $r(c)$ by r , with the argument c implied. The matrix $K(\xi, \alpha)$ is independent of α because firstly, $H^\top M(s)H$ is a function of $\beta - \alpha$, and secondly, because $\Gamma(\theta)$ is symmetric about the line $\langle o, c \rangle$ through the origin o with direction α . The off-diagonal elements of $K(\xi, \alpha)$ are zero because the off-diagonal elements of $H^\top M(s)H$ are odd functions of $\beta - \alpha$.

If θ is in $\text{int}(T_0)$, $\text{int}(T_1)$ or $\text{int}(T_2)$, then $\Gamma(\theta)$ consists of a single arc parameterised by β as specified by (19) or (20). If θ is in $\text{int}(T_0)$ or $\text{int}(T_1)$, then it follows from (27), (28), (29) and (30) that

$$\begin{aligned} K_{11}(\xi, \alpha) &= (2\sigma^2)^{-1}(1 + 2r^{-2}\xi^2 + r^{-1}(4\xi + r \cos(\mu))\mu^{-1} \sin(\mu)), \\ K_{12}(\xi, \alpha) &= K_{21}(\xi, \alpha) = 0, \\ K_{22}(\xi, \alpha) &= (2\sigma^2)^{-1}\xi^2(1 - \cos(\mu)\mu^{-1} \sin(\mu)), \quad q(\xi, \alpha) \in \text{int}(T_i), i = 0, 1, \end{aligned} \quad (31)$$

for an appropriate choice of the angle μ . If $q(\xi, \alpha)$ is in $\text{int}(T_0)$, then $\mu = \pi$. If $q(\xi, \alpha)$ is in $\text{int}(T_1)$, then μ is given by (11), with $R = R_1$.

If θ is in $\text{int}(T_2)$, then

$$\begin{aligned} K_{11}(\xi, \alpha) &= (2\sigma^2)^{-1}(1 + 2r^{-2}\xi^2 - (r(\pi - \mu))^{-1}(4\xi + r \cos(\mu)) \sin(\mu)), \\ K_{12}(\xi, \alpha) &= K_{21}(\xi, \alpha) = 0, \\ K_{22}(\xi, \alpha) &= (2\sigma^2)^{-1}\xi^2(1 + (\pi - \mu)^{-1} \cos(\mu) \sin(\mu)), \quad q(\xi, \alpha) \in \text{int}(T_2), \end{aligned} \quad (32)$$

where μ in (32) is given by (11) with $R = R_2$.

If θ is an element of $\text{int}(T_3)$, then $\Gamma(\theta)$ consists of two arcs parameterised as specified by (21) and (22). With μ_1 and μ_2 as defined in the lines preceding (21) and (22), the entries of $K(\xi, \alpha)$ are given by

$$\begin{aligned} K_{11}(\xi, \alpha) &= \frac{r^2 + 2\xi^2}{2r^2\sigma^2} + \frac{(4\xi + r \cos(\mu_1)) \sin(\mu_1) - (4\xi + r \cos(\mu_2)) \sin(\mu_2)}{2r(\mu_1 - \mu_2)\sigma^2}, \\ K_{12}(\xi, \alpha) &= K_{21}(\xi, \alpha) = 0, \\ K_{22}(\xi, \alpha) &= (2(\mu_1 - \mu_2)\sigma^2)^{-1}\xi^2(\mu_1 - \mu_2 - \cos(\mu_1) \sin(\mu_1) + \cos(\mu_2) \sin(\mu_2)). \end{aligned} \quad (33)$$

4.3 Continuity of the metric

The approximation $K(\xi, \alpha)$ to the Fisher-Rao metric is continuous as a function of ξ at the boundaries between the sets $\text{int}(T_i)$, $0 \leq i \leq 3$. For example, if $\text{int}(T_0)$ and $\text{int}(T_1)$ are non-empty, then the boundary between the two sets is given by

$$\|c\| = \xi_1 \equiv \frac{1}{2}(4a^2 R_1^{-1} - R_1).$$

The angle μ in (31) is a function of $\xi = \|c\|$. The continuity of $K(\xi, \alpha)$ at the boundary between $\text{int}(T_0)$ and $\text{int}(T_1)$ follows because

$$\lim_{\xi \rightarrow \xi_1^+} \mu(\xi) = \pi.$$

If $\text{int}(T_0)$ and $\text{int}(T_2)$ are nonempty, then $\text{int}(T_1)$ is empty and the boundary between $\text{int}(T_0)$ and $\text{int}(T_2)$ is given by

$$\|c\| = \xi_2 \equiv \frac{1}{2}(R_2 - 4a^2 R_2^{-1}).$$

The angle μ in (32) is a function of $\xi = \|c\|$, and the continuity of $K(\xi, \alpha)$ at the boundary between $\text{int}(T_0)$ and $\text{int}(T_2)$ follows because

$$\lim_{\xi \rightarrow \xi_2^+} \mu(\xi) = 0.$$

Suppose that $\text{int}(T_2)$ and $\text{int}(T_3)$ are non-empty. The continuity of $K(\xi, \alpha)$ at the boundary between $\text{int}(T_2)$ and $\text{int}(T_3)$ is checked as follows. If (ξ_1, α_1) is a point in this boundary, then it follows from (17) and (18) that

$$\xi_1 = 2^{-1}(4a^2R_1^{-1} - R_1) > 2^{-1}|R_2 - 4a^2R_2^{-1}| \geq 0.$$

Next, suppose that $\xi \rightarrow \xi_1+$. It follows from (10) that $\mu_1 \leftarrow \pi$. On substituting $\mu_1 = \pi$ into (33), the equations (32) for $K(\xi, \alpha)$ in $\text{int}(T_2)$ are obtained. It follows that $K(\xi, \alpha)$ is continuous across the boundary between $\text{int}(T_3)$ and $\text{int}(T_2)$ as claimed. A similar argument applies if $\text{int}(T_1)$ and $\text{int}(T_3)$ are non-empty.

5 Isometries

It has been shown in Section 3.1 that each non-empty set $\text{int}(T_i)$ can be identified with a disk ($i = 0$) or an annulus ($i = 1, 2$) or the exterior of a closed disk in \mathbb{R}^2 ($i = 3$). In Section 4 it has been shown that each non-empty set $\text{int}(T_i)$ is equipped with a Riemannian metric K which closely approximates the Fisher-Rao metric on $\text{int}(T_i)$. In this section subsets $W_i(j)$ for $1 \leq j \leq \lambda_i$ are found in each non-empty set $\text{int}(T_i)$ such that $W_i(j)$ is isometric to a surface of revolution D_i in \mathbb{R}^3 and such that

$$\text{int}(T_i) \setminus W_i \equiv \bigcup_{j=1}^{\lambda_i} W_i(j)$$

has a small but non-zero area. The Riemannian metric on D_i is induced by the Euclidean metric on \mathbb{R}^3 . In Section 6 it is shown that D_i can be mapped to a subset of the Euclidean plane by a function that closely approximates to an isometry.

A general expression for the isometry from $W_i(j)$ to D_i is obtained in Section 5.1 and examples of these isometries are given in Section 5.2.

5.1 Surface of revolution in \mathbb{R}^3

Let $\text{int}(T_i)$ be non-empty, and let polar coordinates ξ, α be chosen for $\text{int}(T_i)$ as described in Section 4.2. Let $\xi_{i,\min}$ and $\xi_{i,\max}$ be defined for T_i non-empty by

$$\begin{aligned} \xi_{i,\min} &= \inf\{\|c\|, c \in T_i\}, \\ \xi_{i,\max} &= \sup\{\|c\|, c \in T_i\}. \end{aligned}$$

Let $\xi_{i,1}, \xi_{i,2}$ be real numbers such that

$$\xi_{i,\min} \leq \xi_{i,1} < \xi_{i,2} \leq \xi_{i,\max}, \tag{34}$$

and let W_i be the subset of $\text{int}(T_i)$ defined by

$$W_i = \{q(\xi, \alpha), \xi_{i,1} \leq \xi \leq \xi_{i,2}\}.$$

Additional constraints on $\xi_{i,1}$ and $\xi_{i,2}$ will be obtained later in this subsection. It is shown below that if (34) holds and if the additional constraints hold, then there exists a division

of W_i into λ_i subsets $W_i(j)$, $1 \leq j \leq \lambda_i$ such that each $W_i(j)$ is isometric to a surface of revolution in \mathbb{R}^3 . The key properties of $K(\xi, \alpha)$ on which this result depends are firstly that $K(\xi, \alpha)$ is a diagonal matrix and secondly, $K(\xi, \alpha)$ is independent of α . It is convenient to write $K(\xi)$ in place of $K(\xi, \alpha)$.

The following detailed calculation is adapted from Struik (1961). The squared length element ds^2 on $\text{int}(T_i)$ under the Riemannian metric $K(\xi)$ is

$$ds^2 = K_{11}(\xi)d\xi^2 + K_{22}(\xi)d\alpha^2. \quad (35)$$

To simplify the notation, the index i is omitted from W_i , $\xi_{i,1}$ and $\xi_{i,2}$, except where the omission causes ambiguity. Let Cartesian coordinates x, y, z be chosen in \mathbb{R}^3 , let λ be a strictly positive integer, and consider the following function from W to a surface D in \mathbb{R}^3 ,

$$(\xi, \alpha)^\top \mapsto (\rho(\xi) \cos(\lambda\alpha), \rho(\xi) \sin(\lambda\alpha), z(\xi))^\top, \quad \xi_1 \leq \xi \leq \xi_2, 0 \leq \alpha < 2\pi, \quad (36)$$

where the functions $\xi \mapsto \rho(\xi)$ and $\xi \mapsto z(\xi)$ are determined using the condition that (36) preserve the squared length element (35). A full account of this result is given by Struik (1961) for the case $\lambda = 1$. The squared length element on the surface in \mathbb{R}^3 parameterised by (ξ, α) , as shown in (36), is

$$(d(\rho(\xi) \cos(\lambda\alpha)))^2 + (d(\rho(\xi) \sin(\lambda\alpha)))^2 + (dz(\xi))^2$$

which reduces to

$$((d\rho/d\xi)^2 + (dz/d\xi)^2) d\xi^2 + \lambda^2 \rho(\xi)^2 d\alpha^2. \quad (37)$$

On equating the right hand sides of (35) and (37) it follows that

$$\begin{aligned} \rho(\xi) &= \lambda^{-1} K_{22}(\xi)^{1/2}, & \xi_1 \leq \xi \leq \xi_2, \\ z(\xi) &= \int_{\xi_1}^{\xi} \left(K_{11}(\xi') - (4\lambda^2 K_{22}(\xi'))^{-1} (dK_{22}/d\xi')^2 \right)^{1/2} d\xi', & \xi_1 \leq \xi \leq \xi_2. \end{aligned} \quad (38)$$

It is assumed in (38) that

$$K_{11}(\xi) - (4\lambda^2 K_{22}(\xi))^{-1} (dK_{22}/d\xi)^2 \geq 0, \quad \xi_1 \leq \xi \leq \xi_2. \quad (39)$$

It is necessary to choose ξ_1 near to ξ_{min} , ξ_2 near to ξ_{max} and λ sufficiently large to ensure that (39) holds. If (39) does hold, then it follows from (36) that D is a surface of revolution in \mathbb{R}^3 such that the axis of revolution is the z axis.

At this point the subscript i is reintroduced. Thus ξ_1 and ξ_2 are replaced by $\xi_{i,1}$, $\xi_{i,2}$, respectively, and λ is replaced by λ_i . If $i = 0$, then (39) holds for $\lambda_0 = 1$, $\xi_{0,1} = \xi_{0,min}$ and $\xi_{0,2} = \xi_{0,max}$. If $i = 1$ and $\xi_{1,1} = \xi_{1,min}$, then a calculation using Mathematica shows that there is no finite value of λ_1 for which (39) holds. In order to obtain the inequality (39) for a finite value of λ_1 , it is necessary to ensure that $\xi_{1,1} > \xi_{1,min}$. Similarly, if $i = 2$, then it is necessary to ensure that $\xi_{2,1} > \xi_{2,min}$. If $i = 3$, the conditions $\xi_{3,1} > \xi_{3,min}$ and $\xi_{3,2} < \xi_{3,max}$ are required. To summarise, $\xi_{i,1}$ and $\xi_{i,2}$ are required to satisfy the following constraints.

$$\begin{aligned} i = 0 : & \quad \xi_{i,min} \leq \xi_{i,1} < \xi_{i,2} \leq \xi_{i,max}, \\ i = 1, 2 : & \quad \xi_{i,min} < \xi_{i,1} < \xi_{i,2} \leq \xi_{i,max}, \\ i = 3 : & \quad \xi_{i,min} < \xi_{i,1} < \xi_{i,2} < \xi_{i,max}. \end{aligned}$$

Once the values of $\xi_{i,1}$ and $\xi_{i,2}$ are chosen, a value for $\lambda \equiv \lambda_i$ can be chosen.

Let ι be the function from W_i to D_i defined by (36), and let $b = (b_1, b_2, b_3)^\top$ be a point in D_i . The set $\iota^{-1}(b)$ in W_i is of the form

$$\{q(\xi, \alpha_1), \dots, q(\xi, \alpha_\lambda)\}, \quad (40)$$

where $\alpha_1, \dots, \alpha_\lambda$ are distinct angles in $[0, 2\pi)$. The value of ξ is obtained by numerical solution of the equation $b_3 = z(\xi)$. The λ angles $\alpha_1, \dots, \alpha_\lambda$ are obtained by solving the following equation for α ,

$$(\cos(\lambda\alpha), \sin(\lambda\alpha)) = (b_1^2 + b_2^2)^{-1/2}(b_1, b_2)^\top, \quad 0 \leq \alpha < 2\pi. \quad (41)$$

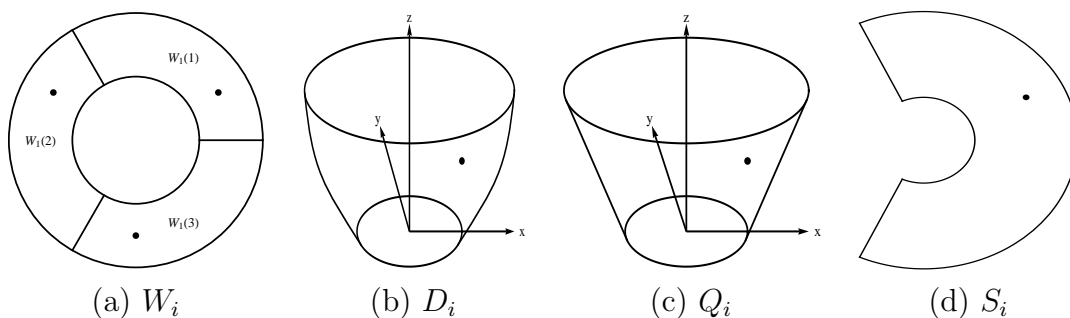


Figure 4: The spaces W_i , D_i , Q_i and S_i are used to construct an approximation to the space $\text{int}(T_i)$ equipped with the Fisher-Rao metric. a) In this example, W_i is an annulus contained in $\text{int}(T_i)$ such that $\text{int}(T_i) \setminus W_i$ has a small area. The annulus W_i is divided into three parts $W_i(j)$, $1 \leq j \leq 3$. Each part $W_i(j)$ is a Riemannian manifold under the approximation K to the Fisher-Rao metric. b) Each $W_i(j)$ is mapped isometrically onto a surface of revolution D_i in \mathbb{R}^3 . Each point in D_i is the image of three points in W_i , one point from each of the $W_i(j)$, for example as shown in (a). c) The surface of revolution D_i is approximated by a frustum Q_i of a right circular cone. d) The frustum Q_i is cut along a generator and rolled out to obtain a subset S_i of the Euclidean plane \mathbb{R}^2 . The resulting function, $W_i(j) \rightarrow S_i$ closely approximates to an isometry for $j = 1, 2, 3$.

It follows from (40) and (41) that W_i can be divided into the following subsets $W_i(j)$,

$$W_i(j) = \{q(\xi, \alpha), \xi_{i,1} \leq \xi \leq \xi_{i,2}, \pi(j-1)/\lambda_i \leq \alpha < 2\pi j/\lambda_i\}, \quad 1 \leq j \leq \lambda_i,$$

such that the function (36) is an isometry from $W_i(j)$ to D_i for $1 \leq j \leq \lambda_i$. The resulting function from W_i to D_i is an example of a local isometry. An example of a division of W_i into three parts $W_i(j)$ for $1 \leq j \leq 3$ is shown in Fig. 4a.

5.2 Examples of isometries

On setting $\mu = \pi$ in (31), and using (6) to substitute for r^2 , it follows that

$$K(\xi, \alpha) = \frac{1}{2\sigma^2} \begin{pmatrix} (4a^2 + 3\xi^2)/(4a^2 + \xi^2) & 0 \\ 0 & \xi^2 \end{pmatrix}, \quad q(\xi, \alpha) \in \text{int}(T_0). \quad (42)$$

The values of $\xi_{0,1}$ and $\xi_{0,2}$ are given by

$$\begin{aligned}\xi_{0,1} &= 0, \\ \xi_{0,2} &= \min \left\{ \frac{1}{2}(4a^2 R_1^{-1} - R_1), \frac{1}{2}(R_2 - 4a^2 R_2^{-1}) \right\}.\end{aligned}$$

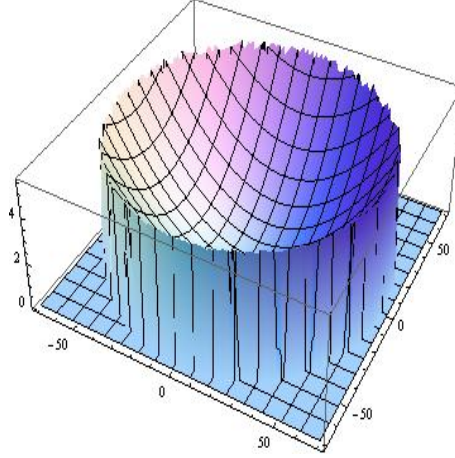


Figure 5: The surface D_0 in \mathbb{R}^3 for $a = 400$, $R_1 = 600$, $R_2 = 900$ and $\sigma = 1$.

The manifold W_0 is embedded isometrically as a surface of revolution D_0 in \mathbb{R}^3 by an equation of the form (36) with $\lambda = 1$. The functions $\xi \mapsto \rho(\xi)$ and $\xi \mapsto z(\xi)$ are defined by

$$\begin{aligned}\rho(\xi) &= \left(\sqrt{2}\sigma\right)^{-1} \xi, & \xi_{0,1} \leq \xi \leq \xi_{0,2}, \\ z(\xi) &= \sigma^{-1}((\xi^2 + 4a^2)^{1/2} - 2a), & \xi_{0,1} \leq \xi \leq \xi_{0,2}.\end{aligned}$$

An example of a surface D_0 is shown in Fig. 5. The surface D_0 is the curved bowl shaped region. It does not include the shaded quadrilateral at the base of the figure. The z axis is the axis of rotational symmetry of the bowl. The origin is at the lowest point of the bowl on the z axis. The x , y , z coordinates of points on D_0 are given in terms of $\rho(\xi)$, $z(\xi)$ and an angle α by the right hand side of (36). The x , y and z axes are parallel to the appropriate edges of the cuboid in Fig. 5.

If $i = 1, 2$ or 3 , then there appears to be no closed form expression for the function $\xi \mapsto z(\xi)$. In practice, this is not an obstacle because the function can be estimated numerically for given values of a , R_1 , R_2 and σ . An example of a surface D_2 is shown in Fig. 6. The surface D_2 is the curved region which approximates to the frustum of a right circular cone. It does not include the shaded quadrilateral at the base of the figure. The x , y , z coordinates of points on D_2 are given in terms of the appropriate functions $\rho(\xi)$, $z(\xi)$ and an angle α by the right hand side of (36). The x , y and z axes are parallel to the appropriate edges of the cuboid in Fig. 6.

6 Digital Image Based on Lines

It was shown in Section 5 that each non-empty set $\text{int}(T_i)$ contains a subset W_i which can be mapped by a local isometry to a surface of revolution D_i in \mathbb{R}^3 . Each set W_i is

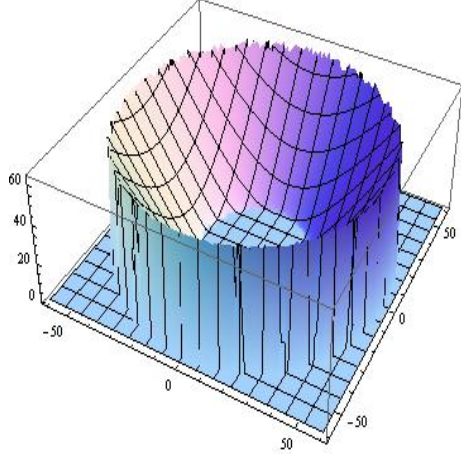


Figure 6: The surface D_2 in \mathbb{R}^3 for $a = 400$, $R_1 = 600$, $R_2 = 900$, $\sigma = 1$ and $\lambda = 4$.

partitioned into subsets $W_i(j)$ for $1 \leq j \leq \lambda_i$ such that $W_i(j)$ is mapped isometrically to D_i . In this section it is shown that each surface of revolution D_i can be closely approximated by a part Q_i of a right circular cone. The surface Q_i is isometric to a subset S_i of the Euclidean plane obtained by cutting Q_i along a generator and then flattening it out. The resulting function

$$S_i \rightarrow Q_i \rightarrow D_i \rightarrow W_i(j)$$

is an approximate isometry from S_i , equipped with the Euclidean metric to $W_i(j)$, equipped with the approximation to the Fisher-Rao metric inherited from $\text{int}(T_i)$, to S_i . The spaces W_i , D_i , Q_i and S_i are illustrated in Fig. 4. It is convenient to make λ_i identical copies of S_i , one copy for each set $W_i(j)$ for $1 \leq j \leq \lambda_i$. The copies are labeled $S_i(j)$, $1 \leq j \leq \lambda_i$. It is straightforward to digitise each set $S_i(j)$ by choosing pixels at the vertices of a square grid in $S_i(j)$, to obtain digital images $\tilde{S}_i(j)$ for $1 \leq j \leq \lambda_i$. The individual pixels in $\tilde{S}_i(j)$ correspond to projected lines in the original catadioptric image. The trace transform is used to assign values to these pixels.

The approximation to the surface of revolution D_i is described in Section 6.1. The set S_i and the digital images $\tilde{S}_i(j)$ are described in Section 6.2. The trace transform is described in Section 6.3.

6.1 Approximation to the surface of revolution

If $i = 1, 2$ or 3 , then each non-empty surface of revolution D_i is bounded by two circles. Each circle is centred on the z axis and is contained in a plane parallel to the x, y plane. It follows that the two circles are contained in a unique right circular cone or in a right circular cylinder, such that the axis of the cone or cylinder coincides with the z axis. Let Q_i be the finite part of the cone bounded by the two circles. The surface Q_i is an example of a frustum. If $i = 0$ and D_0 is non-empty, then the boundary of D_0 consists of a single circle. There is a unique right circular cone which contains the boundary of D_0 and which has a vertex at the point $(0, 0, 0)^\top$ in D_0 . Let Q_0 be the finite part of this cone bounded by the boundary of D_0 .

Each set Q_i is an approximation to D_i . The accuracy to which Q_i approximates D_i is measured as follows. Let $b_i(1), b_i(2)$ be points of Q_i on the same generator of Q_i , but as far from each other as possible. If $i = 1, 2$ or 3 then $b_i(1)$ and $b_i(2)$ are on different components of the common boundary contained in $D_i \cap Q_i$. If $i = 0$, then without loss of generality, $b_0(1) = (0, 0, 0)^\top$ and $b_0(2)$ is on the common boundary contained in $D_0 \cap Q_0$. The accuracy to which Q_i approximates D_i is measured by the ratio of the geodesic distance between $b_i(1)$ and $b_i(2)$ in D_i to the geodesic distance between $b_i(1)$ and $b_i(2)$ in Q_i . The latter distance is $\|b_i(2) - b_i(1)\|$, where $\|\cdot\|$ is the Euclidean metric in \mathbb{R}^3 . Experimental values of this ratio are reported in Section 7.4.

6.2 Digital image for projected lines

Each non-empty surface Q_i is cut along the generator corresponding to the curve $\alpha = 0$ in D_i and then unrolled to yield a subset S_i of \mathbb{R}^2 . The resulting function $j : S_i \rightarrow Q_i$ is an isometry. If $i = 0$, then S_i is a sector of a disk. If $i = 1, 2$ or 3 , then S_i is part of an annulus, for example as shown in Fig. 7.

Let ν be the half open angle of the cone containing Q_i , that is, the angle between a generator of the cone and the axis of the cone. The line segments AB and DC in Fig. 7 intersect at the angle ψ given by $\psi = 2\pi \sin(\nu)$. Let coordinates be chosen in \mathbb{R}^3 such that the vertex of the cone containing Q_i is at the origin and the axis of the cone coincides with the z -axis. Let Q_i extend from the plane $z = z_{min}$ to the plane $z = z_{max}$. A general point in Q_i is given by

$$(z \tan(\nu) \cos(\beta), z \tan(\nu) \sin(\beta), z)^\top, \quad z_{min} \leq z \leq z_{max}, 0 \leq \beta < 2\pi.$$

Let $(u_1, u_2)^\top$ be the corresponding point in S_i . Then it follows that

$$\begin{aligned} \beta &= \operatorname{cosec}(\nu) \tan^{-1}(u_2/u_1), \\ z &= \sin(\nu) (u_1^2 + u_2^2)^{1/2}. \end{aligned}$$

Let L be a square lattice in \mathbb{R}^2 such that the squares formed by the points of L are of size $\sqrt{2} \times \sqrt{2}$. Any given point of \mathbb{R}^2 is within a distance 1 of at least one element of L ,

$$\sup_{e \in \mathbb{R}^2} \inf_{v \in L} \|e - v\| = 1.$$

Let $h : Q_i \rightarrow D_i$ be the function defined such that $h(b)$ is the nearest point in D_i to b . The sample points in D_i are defined by

$$h(j(L \cap S_i)). \tag{43}$$

The set \tilde{S}_i of pixels is defined by

$$\tilde{S}_i = L \cap S_i, \quad 0 \leq i \leq 3.$$

Finally, the sample points (43) in D_i are mapped to to the subset $W_i(j)$ of $\operatorname{int}(T_i)$ defined in Section 5.1. Each point in (43) corresponds to λ_i points in W_i , such that each subset $W_i(j)$ of W_i contains exactly one of the points. The set of pixels associated with $W_i(j)$ is $\tilde{S}_i(j)$, $1 \leq j \leq \lambda_i$.

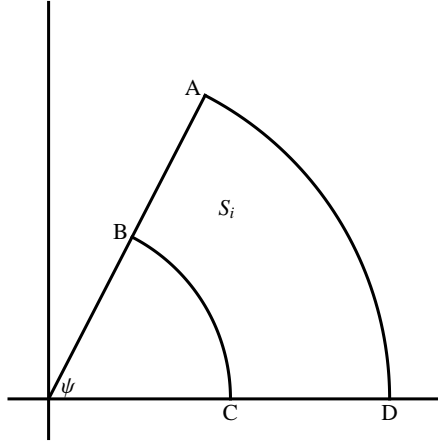


Figure 7: A surface $S_i = ABCD$ in \mathbb{R}^2 which corresponds to the subset Q_i of a right circular cone in \mathbb{R}^3 .

6.3 Pixel values

The trace transform (Kadyrov and Petrou 2001) is used to assign values to the pixels in the digital images $\tilde{S}_i(j)$ obtained in Section 6.2. The trace transform is usually defined for straight lines in an image. In this application the definition of the trace transform is extended to the projected lines in a paracatadioptric image as follows. Let u be a pixel in $\tilde{S}_i(j)$, let $\theta \equiv \theta(u)$ be the corresponding point in $\text{int}(T_i)$ and let $C(\theta)$ be the projected line in the paracatadioptric image I . Let $\Gamma(\theta) = C(\theta) \cap I$ and let $N(\theta)$ be the set of pixels in I that are obtained by rounding the coordinates of the points in $\Gamma(\theta)$ to the nearest integer. The value of a pixel (m, n) in I is I_{mn} . The trace transform $\tau(\theta)$ is defined by

$$\tau(\theta) = |N(\theta)|^{-1} \sum_{(m,n) \in N(\theta)} I_{mn}. \quad (44)$$

The trace transform is closely related to the Radon transform. The Radon transform is invertible, and thus preserves all the information in the original image. It is plausible that the continuous version of the trace transform (44) is also invertible and thus information preserving.

7 Detection of Projected Lines

The theory described in Sections 3 to 6 is applied to the detection of projected lines in paracatadioptric images. The calibration of a paracatadioptric image is described in Section 7.1. Some functions used in the algorithms for line detection are described in Section 7.2. Three algorithms for detecting projected lines are described in Section 7.3. Two of the algorithms are based on the digital version $\tilde{S}_i(j)$ of the parameter space for projected lines, as described in Sections 6.2 and 6.3. Both algorithms are based on a standard operator in image processing, namely the Sobel operator (Gonzalez and Woods 2002). It is possible to apply the Sobel operator in a straightforward way, because the Fisher-Rao metric on each digital image $\tilde{S}_i(j)$ is closely approximated by the Euclidean metric. The third algorithm is based on the Hough detector and a circle fitting method

taken from the literature. Experiments to compare the three algorithms are described in Section 7.4.

7.1 Calibration

The paracatadioptric system used in the experiments was a ParaShot device from Remote-Reality. The manufacturer provided the parameter values $R_2 = 4.25$ cm and $\chi = 105^\circ$, where R_2 , χ are as shown in Fig. 8. The calibration of the system was carried out using the methods described by Kang (2000). In detail, the parameter a in (1) was calculated using the equation

$$a = \frac{1}{2} R_2 \cot(\chi/2).$$

The principal point was estimated by the centre of a circle that was fitted to the outer boundary of the image. The estimates of a and the principal point were checked on a suitable image using a publicly available toolbox for calibrating omnidirectional cameras (Scaramuzza 2011).

The Hough algorithm for line detection requires a distortion of the paracatadioptric image to produce a sphere such that each point on the sphere corresponds to an incoming ray. In detail, let S be a sphere of radius $2a$ centred at the focal point F of the mirror. Each image point x arises from a ray originally directed towards F , prior to reflection by the mirror. Let $l(x)$ be the line in \mathbb{R}^3 that contains the incoming ray and let $g(x)$ be the point in $l(x) \cap S$ on the same side of F as the incoming ray. The function $x \mapsto g(x)$ can be calculated for any given value of x , once the value of a is known.

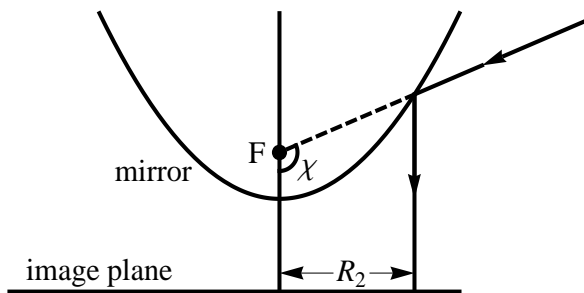


Figure 8: Field of view of a catadioptric system.

7.2 Functions

The following functions, `sobel`, `top` and `centre`, are required by the two algorithms which use the digital images $\tilde{S}_i(j)$ to detect projected lines.

i) `sobel`

input: a digital image I .

output: a binary image B obtained as follows. The Sobel edge operator is applied to I . Let the resulting image of the magnitudes of the Sobel gradients be G , let the

size of G be $n_1 \times n_2$ and let t be a threshold defined by

$$t = 2 \left(\frac{1}{n_1 n_2} \sum_{i,j=1}^{n_1, n_2} G_{ij}^2 \right)^{1/2}. \quad (45)$$

The binary image B is defined by $B_{ij} = 1$ if $G_{ij} \geq t$ and $B_{ij} = 0$ otherwise, for $1 \leq i \leq n_1$ and $1 \leq j \leq n_2$. The threshold t is obtained from the MATLAB implementation of the Sobel operator. See also Pratt (2007).

ii) top

input: a list of digital images and a non-negative integer n .

output: a list of the n pixels with the largest values in the combined images.

iii) centres

input: a list L of triples (i, j, r) such that each (i, j) is a pixel in a digital image I , and the pixel value I_{ij} is equal to r .

output: Let A_k for $1 \leq k \leq m$ be the maximal 8-connected components of the pixels (i, j) obtained from the triples in L and let u_k be the pixel in A_k with the largest value. The list u_k for $1 \leq k \leq m$ is output.

7.3 Algorithms

It is assumed that the paracatadioptric imaging system is calibrated, in that the parameter a in (1) which describes the shape of the mirror and the principal point o at which the axis of the mirror intersects the image plane are both known. It is also assumed that the bounding circles C_1, C_2 of the paracatadioptric image I are centred at o and have known radii R_1, R_2 . The value 1 is assigned to the parameter σ in (24).

The pixel values in digital images $\tilde{S}_i(j)$ are obtained as described in Section 6.3. It is convenient to include the image I in the notation and to write $\tilde{S}_i(j, I)$ in place of $\tilde{S}_i(j)$. In Algorithm 1 the Sobel edge operator is applied to the paracatadioptric image and then the trace transform of the Sobel image is obtained. In Algorithm 2 the order is reversed: first, the trace transform is applied to the paracatadioptric image and then the Sobel edge operator is applied to the trace transform image.

Algorithm 1

input: a paracatadioptric image I and a positive integer N .

output: let M' be the list of images M'_{ij} defined by

$$M'_{ij} = \tilde{S}_i(j, \text{sobel}(I)), \quad 1 \leq j \leq \lambda_i, 0 \leq i \leq 3.$$

The output is

$$\text{centres}(\text{top}(M', N)).$$

Algorithm 2

input: a paracatadioptric image I and a positive integer N .

output: let M'' be the list of images M''_{ij} defined by

$$M''_{ij} = \text{sobel}(\tilde{S}_i(j, I)), \quad 1 \leq j \leq \lambda_i, 0 \leq i \leq 3.$$

The output is

$$\text{centres}(\text{top}(M'', N)).$$

Algorithm 3 is constructed from the Hough detector of Ying and Hu (2004) and the circle fitting method of Barreto and Araujo (2006). Edge points are found in the paracatadioptric image I using the Sobel operator. Each edge point x corresponds to a point $g(x)$ on the sphere S of radius $2a$ centred at the focal point F of the mirror. The definition of $g(x)$ is given in Section 7.1. The family of great circles in S is parameterised by the elevation ψ , which takes values in $[0, \pi/2]$ and the azimuth ϕ which takes values in $[0, 2\pi)$. The point $(0, 0, -a)^\top$ on S corresponds to $\psi = 0$. The Hough space is a hemisphere of S . The Hough accumulators are obtained by dividing each range $[0, \pi/2]$ and $[0, 2\pi)$ into 256 parts.

Algorithm 3

input: a list of edge points in I and a positive integer N .

output: set of great circles.

1. set $B = \text{sobel}(I)$.
2. **for** each pixel x in B with value 1 **do**
3. vote in the Hough accumulator for all planes containing F and $g(x)$
4. **endfor**
5. keep the N accumulators with the largest values
6. **for** each of the N accumulators
7. select the points $g(x)$ near to the corresponding great circle
8. fit a circle to the selected points
9. **endfor**

In step 7 of Algorithm 3, a point $g(x)$ is selected if the distance from $g(x)$ to the plane containing the great circle is less than $a/500$. The complexity of the algorithm is $O(L)$, where L is the number of pixels in the Sobel image B with value 1.

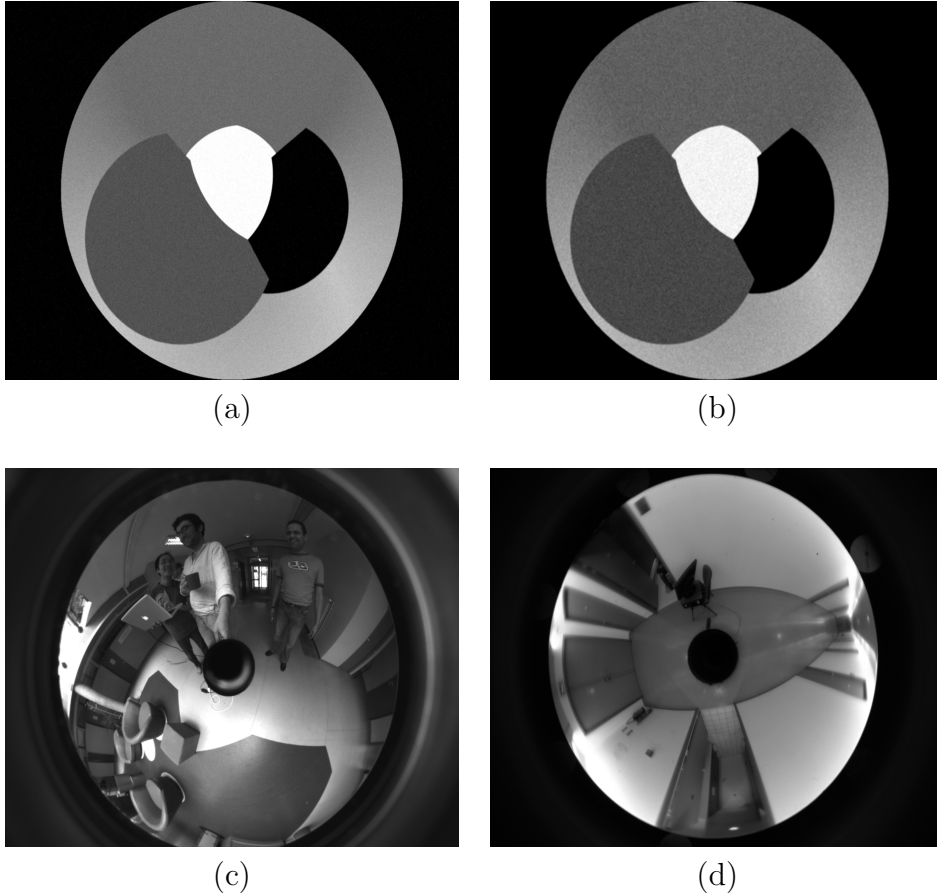


Figure 9: The original images: a) Synthetic1; b) Synthetic2; c) Office2; d) Corridor.

7.4 Experimental results

Experiments were carried out using the four images shown in Fig. 9. The images Synthetic1 in Fig. 9(a) and Synthetic2 in Fig. 9(b) were generated as follows. A computer graphics scene was created using the 3D renderer Blender. White Gaussian noise with zero expected value was added to each pixel and the image was then smoothed using a mask with constant entries. In Synthetic1 the Gaussian noise has a standard deviation of 11.3, the grey scale range is 256 and the mask is of size 3×3 . In Synthetic2 the Gaussian noise has a standard deviation of 22.6, the grey scale range is 256 and the mask is of size 5×5 . The scene was then projected to a plane image with resolution 1360×1024 using a mathematical model for the catadioptric system. Both synthetic images contain nine projections of straight lines. The remaining two images in Fig. 9 are real images, each with the same resolution of 1360×1024 . The two images were obtained using a catadioptric system consisting of the RemoteReality Parashot device coupled with a camera. All four images are uncompressed in order to avoid any artifacts that might arise from compression.

The values of a , the principal point, R_1 , R_2 and the frustum quality for each image are shown in Table 1. The frustum quality is, by definition, the maximum of the ratios of geodesic distances defined at the end of Section 6.1, for those values of i for which the

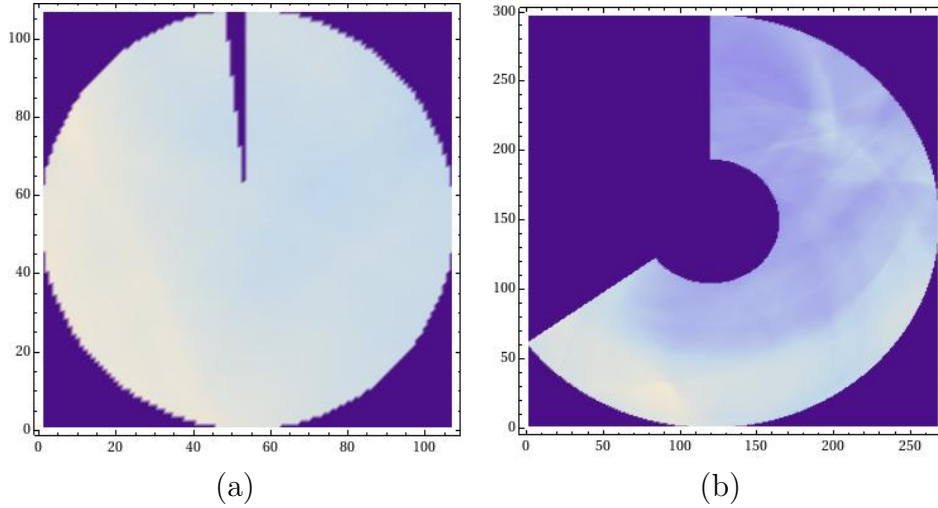


Figure 10: Two digital images $\tilde{S}_i(j)$ obtained from the image Office2 using the trace transform: a) $i = 0, j = 1$; b) $i = 2, j = 1$.

frustum Q_i and the surface of revolution D_i are defined. The approximation to D_i by Q_i is accurate if the frustum quality is near to 1. Two examples of images obtained by cutting the frustum Q_i and then rolling the surface Q_i out onto a plane are shown in Fig. 10. The parameter a and the principal point were checked for the image Corridor using the toolbox published on the web by Scaramuzza (2011). The results were $a = 189.1$ with principal point estimated to be at $(509.8, 672.6)$, in good agreement with Kang’s calibration method (see Section 7.1). In order to use the toolbox it was necessary to take a number of images with the same camera position as for the image Corridor, but with chequer boards included in the scene. These additional images are not shown.

parameter	Synthetic1	Synthetic2	Office2	Corridor
a	102.4	102.4	194.7	189.2
principal point	(512,680)	(512,680)	(539.7,671.5)	(509.8,669.8)
R_1	0	75.5	78.5	75.5
R_2	512	512	507.5	493.2
frustum quality	1.025 ($i = 0$)	1.025 ($i = 0$)	1.012 ($i = 2$)	1.012 ($i = 2$)

Table 1. Values in pixels of a , the principal point, R_1 , R_2 and also the frustum quality for the four images in Fig. 9.

Algorithms 1 and 2 were implemented in Mathematica Version 7.0 and run on an 8 core Intel Xeon CPU with a speed of 2.93GHz and 4 GB of RAM. Algorithm 3 was implemented in MATLAB and run on a 2.4 GHz Core 2 Duo processor.

7.4.1 Algorithm 1 and Algorithm 2

In the case of Algorithm 1, the function sobel was applied to each of the four images in Fig. 9, to produce the four binary images of thresholded Sobel gradients shown in Fig. 11.

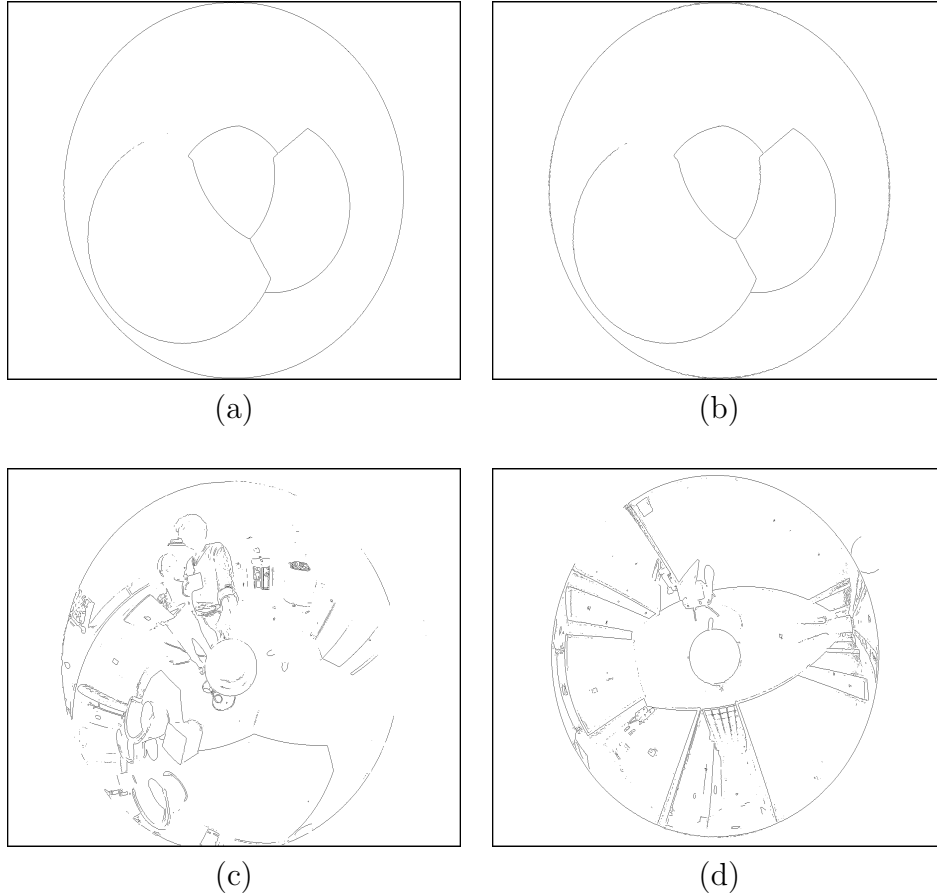


Figure 11: Binary images of thresholded Sobel gradients.

Let N be the number of projected lines found initially by Algorithm 1 and let N_c be the number of projected lines returned by the algorithm. The parameter N is the argument n of the function `top`, as defined in Section 7.2. The parameter N was adjusted to ensure that N_c is of the order 8.

algorithm	parameter	Synthetic1	Synthetic2	Office2	Corridor
1	N	36	75	75	55
1	N_c	7	7	11	10
1	run time (s)	328	321	236	222
2	N	1200	1000	100	90
2	N_c	7	8	7	9
2	run time (s)	338	338	254	237
3	num. projected lines	10	10	10	10
3	run time (s)	1.7	2.0	8.1	9.4

Table 2. Results for all three algorithms.

The values of N , N_c and the run times for Algorithm 1 are shown in Table 2. The run times do not include the time taken to construct the pixels in the digital images $\tilde{S}_i(j)$,

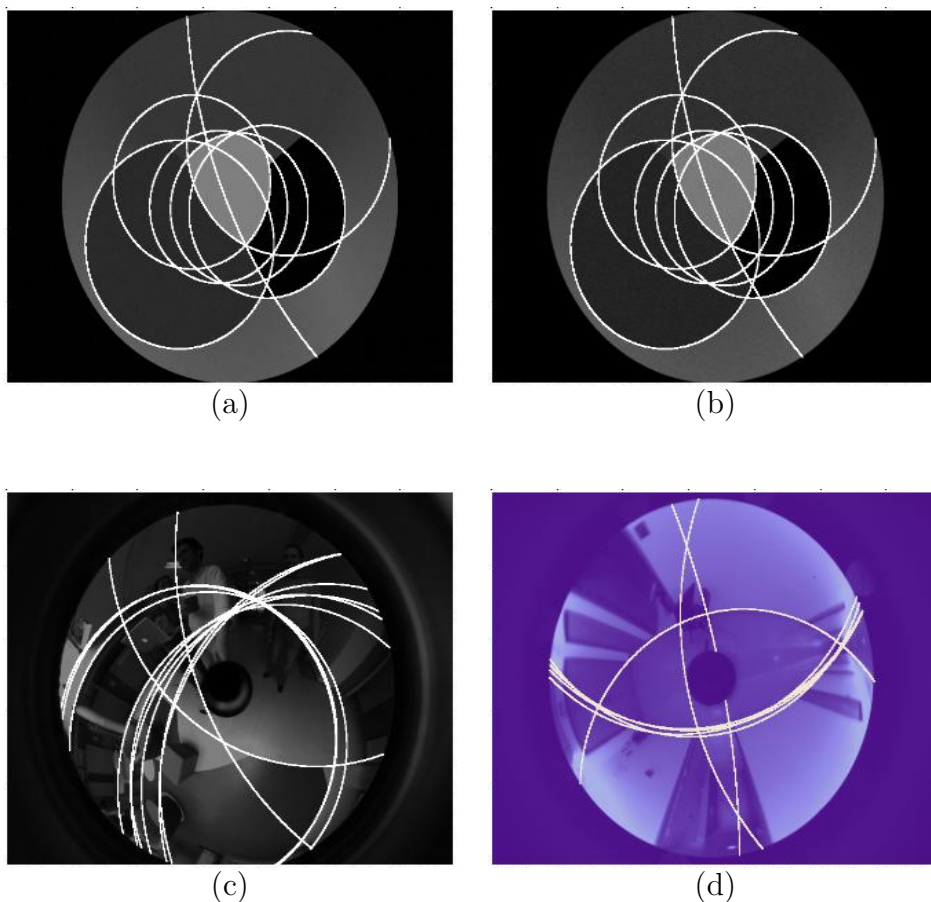


Figure 12: Results of Algorithm 1: a) Synthetic1; b) Synthetic2; c) Office2; d) Corridor. Detected lines are shown in white.

because this task can be carried out offline. The run times also do not include the time to calculate the Sobel images. They do include the time taken for the trace transform which is used to obtain the values of the pixels in $\tilde{S}_i(j)$. In fact, this is a large part of each run time. The four paracatadioptric images are shown in Fig. 12 with the N_c projected lines superposed on each image.

In the case of Algorithm 2, the trace transform was applied to each of the four images in Fig. 9, and the Sobel edge operator was applied to the resulting images. The values of N , N_c and the run times for Algorithm 2 are shown in Table 2. The projected lines detected by Algorithm 2 are shown in Fig. 13.

7.4.2 Algorithm 3

The parameter N which specifies the number of lines returned by Algorithm 3 was set equal to 10. The 10 projected lines are shown superposed on the original images in Fig. 15. The Hough transform space for Synthetic1 and Synthetic2 was of size 210×210 and for Office2 and Corridor it was of size 256×256 . The smaller Hough transform space was better suited to Synthetic1 and Synthetic2 because of their simple structure. The

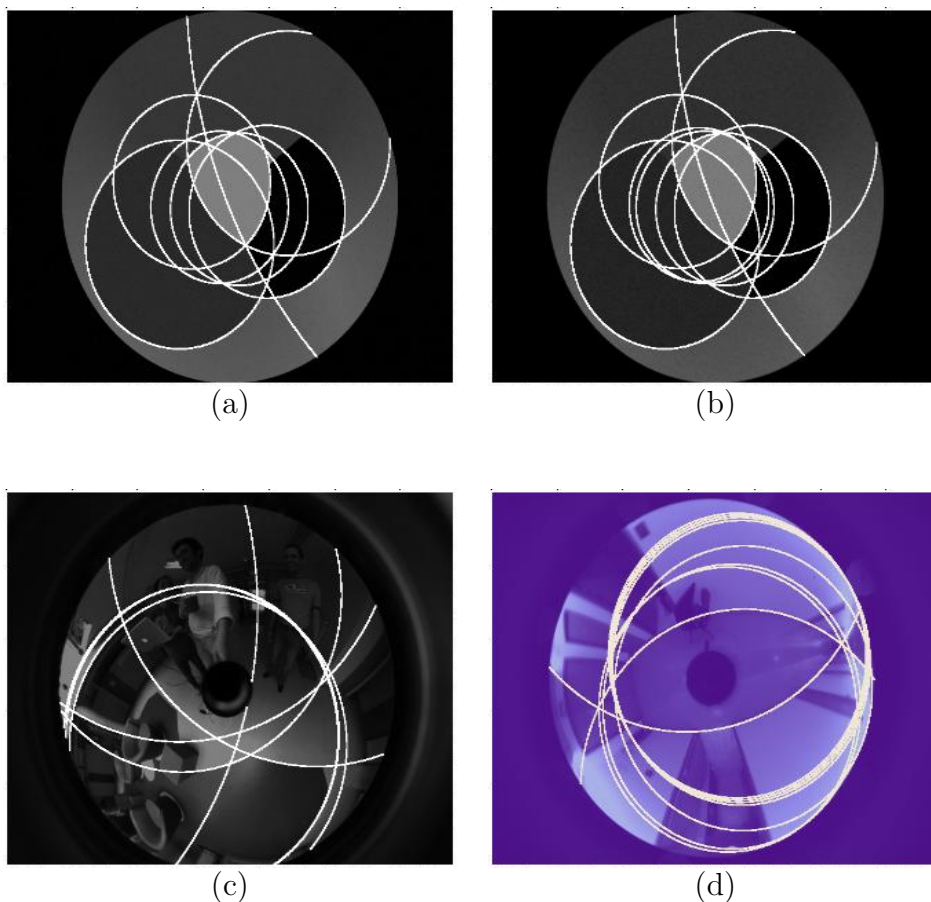


Figure 13: Results of Algorithm 2: a) Synthetic1; b) Synthetic2; c) Office2; d) Corridor. Detected lines are shown in white.

numbers of distinct projected lines and the run times are shown in Table 2. There was no explicit compilation of the MATLAB code prior to the measurement of the run times.

7.5 Discussion

It is apparent from the images shown in Figs 12 and 13 that Algorithm 1 and Algorithm 2 both successfully detect 7 out of the 9 lines in the images Synthetic1 and Synthetic2. The performances of both algorithms are similar for both synthetic images, in spite of the fact that the noise level in Synthetic2 is twice the noise level in Synthetic1. Algorithm 3 performs less well on the synthetic images, in that it detects 3 lines in Synthetic1 and only two lines in Synthetic2. The number of ground truth lines detected by Algorithm 3 is low because the algorithm has a tendency to produce multiple detections of lines, all of which are near to a single ground truth line. In Office2, Algorithm 1 and Algorithm 2 find lines associated with the desks at the bottom of the image and on the left hand side of the image. Both algorithms detect the line on the right hand side of the image where the wall meets the floor. Algorithm 1 is distracted by the bright region above and slightly to the right of the centre of Office2. It detects 6 lines which pass through this region. Algorithm

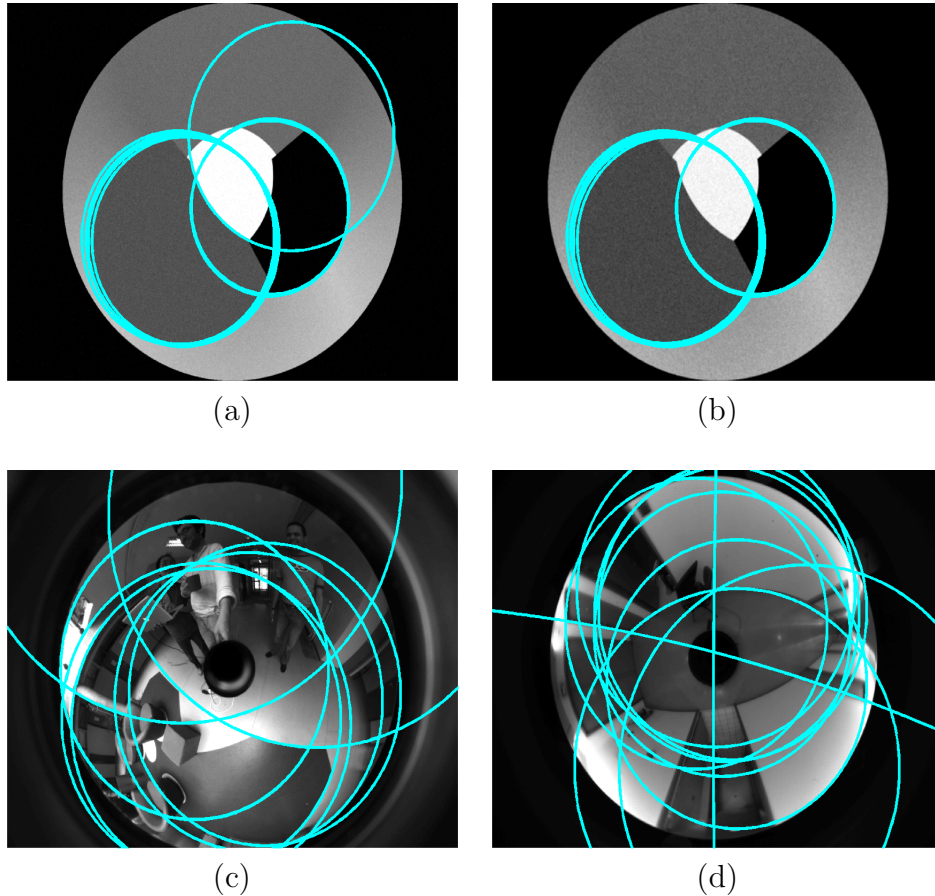


Figure 14: Results of Algorithm 3: a) Synthetic1; b) Synthetic2; c) Office2; d) Corridor. Detected lines are shown in green.

2 is distracted by this region but to a lesser extent, in that it only detects 3 lines passing through the region. Algorithm 3 detects lines in Office2 associated with the edges of the desks but it fails to detect the line on the right hand side, where the wall meets the floor. In Corridor, Algorithm 1 and Algorithm 2 both detect the major lines where the walls meet the floor of the corridor, however in this image both algorithms have a tendency to make multiple detections of lines associated with a single ground truth line. Algorithm 3 finds only one of the two lines where the walls meet the corridor.

A major advantage of Algorithms 1 and 2 is the small number of parameters that they require. In fact, there are only two parameters: the threshold t in the function `sobel`, as defined by (45) and the number N of candidate lines. The number N is a parameter for the function `centres` which is defined in Section 7.2. In practice, t is fixed and the only variable parameter is N . In contrast, Algorithm 3 requires all the parameters that define the Hough accumulators, the parameter t in `sobel` and the number N of projected lines that are returned by the algorithm. It is likely that the performance of Algorithm 3 can be improved for particular images by adjusting the size and shape of the Hough accumulators, however, these adjustments are complicated, in that many parameters are involved, and their effects on the performance of Algorithm 3 on new images are likely to be unpredictable.

The runtimes for Algorithm 1 and Algorithm 2, as shown in Table 2, are much greater than the run times for Algorithm 3. It is likely that these large run times could be reduced by coding Algorithm 1 and Algorithm 2 in a programming language such as Fortran or C++.

8 Conclusion

A Fisher-Rao metric is obtained for the parameterised space of projected lines in a paracatadioptric image. The parameter space is divided into parts such that on each part the Fisher-Rao metric is closely approximated by the Euclidean metric. Each part is digitised by selecting pixels at the vertices of a square grid. The pixel values are obtained by applying the trace transform to the corresponding projected lines in the original paracatadioptric image. The prominent projected lines in the paracatadioptric image are detected by applying standard image processing algorithms to these new digital images. The fact that the Fisher-Rao metric is closely approximated on each part by the Euclidean metric ensures that there are no artifacts arising from the choice of metric.

In this way the effects of the extreme distortions found in paracatadioptric images are removed. It is possible that similar methods can be applied to other catadioptric images, provided the catadioptric system used to obtain the images has a rotational symmetry.

Two new algorithms for detecting projected lines are described. Both of them use the digitised versions of subsets of the parameter space for projected lines, such that on each subset the Fisher-Rao metric is closely approximated by the Euclidean metric. The results obtained from these algorithms are compared with the results obtained from a third algorithm which is based on a Hough detector and a circle fitting method, both of which are taken from the literature. The new algorithms successfully detect the projected lines in a number of images and clearly do better than the third algorithm on synthetic images for which the ground truth is known.

References

1. Amari, S.-I. (1985) *Differential-Geometric Methods in Statistics*. Lecture Notes in Computer Science, vol. 28. Springer.
2. Baker, S. & Nayar, S.K. (1999) A theory of single viewpoint catadioptric image formation. *International Journal of Computer Vision*, vol. 35, no. 2, pp. 175-196.
3. Barreto, J.P. & Araujo, H. (2001) Issues on the geometry of central catadioptric image formation. *Proc. IEEE International Conference on Computer Vision and Pattern Recognition, CVPR2001*, vol. 2, pp. 422-427.
4. Barreto, J.P. & Araujo, H. (2006) Fitting conics to paracatadioptric projections of lines. *Computer Vision and Image Understanding*, vol. 10, no. 3, pp. 151-165. Available at <http://dx.doi.org/10.1016/j.cviu.2005.07.002>
5. Bazin, J.C., Demonceaux, C. & Vasseur, P. (2007a) Fast central catadioptric line extraction. In Martí, J., Benedí, J.M., Mendonça & Serrat, J. (eds) *Pattern Recog-*

- nition and image analysis: third iberian conference, IbPRIA, Part II. Lecture Notes in Computer Science, vol. 4478, pp. 25-32, Springer.*
6. Bazin, J.C., Kweon, I.S., Démonceaux, C. & Vasseur, P. (2007b) Rectangle extraction in catadioptric images. 7th Workshop on Omnidirectional Vision, Camera Networks and Non-Classical Cameras (OMNIVIS'07).
 7. Cover, T.M. & Thomas, J. A. (1991) *Elements of Information Theory*. John Wiley and Sons.
 8. Daniilidis, K., Makadia, A. & Blow, T. (2002) Image processing in catadioptric planes: spatiotemporal derivatives and optical flow computation. *Omnis 2002: Workshop on Omnidirectional Vision*, pp. 3-10.
 9. Duan, F., Wang, L. & Guo, P. (2010) Ransac based ellipse detection with application to catadioptric image calibration. In Wong, K.W., Mendis, S.U. & Bouzerdoum, A. (eds) *Neural Information Processing. Models and Applications - 17th International Conference, ICONIP 2010*. Lecture Notes in Computer Science, vol. 6444, pp. 525-532, Springer.
 10. Gasparini, S. & Caglioti, V. (2011) Line localization from single catadioptric images. *International Journal of Computer Vision*, vol. 94, No. 3, pp. 361-374.
 11. Geyer, C. & Daniilidis, K. (2000) A unifying theory for central panoramic systems and practical implications. In Vernon, D. (ed.) *Computer Vision - ECCV2000*, LNCS vol. 1843, pp. 445-461. Springer.
 12. Geyer, C. & Daniilidis, K. (2001) Catadioptric projective geometry. *International Journal of Computer Vision*, vol. 45, No. 3, pp. 223-243.
 13. Gonzalez, R. C. & Woods, R. E. (2002) *Digital Image Processing*. 2nd edition, Prentice Hall.
 14. Kadyrov, A. & Petrou, M. (2001) The trace transform and its applications. *IEEE Transactions on Pattern Analysis and Machine Intelligence*, vol. 23, Issue 8, pp. 811-821.
 15. Kanatani, K.-I. (1996) *Statistical Computation for Geometric Optimization*. Elsevier.
 16. Kang, S.B. (2000) Catadioptric self-calibration. *IEEE Conference on Computer Vision and Pattern Recognition, CVPR 2000*.
 17. Maybank, S.J. (2004) Detection of image structures using the Fisher information and the Rao metric. *IEEE Transactions on Pattern Analysis and Machine Intelligence*, vol. 26, No. 12, pp. 1579-1589.
 18. Maybank, S.J. (2005) The Fisher-Rao metric for projective transformations of the line. *International Journal of Computer Vision*, vol. 63, No. 3, pp. 191-206.

19. Maybank, S.J. (2007) Application of the Fisher-Rao metric to ellipse detection. *International Journal of Computer Vision*, vol. 72, No. 3, pp. 287-307.
20. Maybank, S.J. (2008) Approximation to the Fisher-Rao metric for the focus of expansion. *Neurocomputing*, vol. 71, pp. 2037-2045.
21. Pinciroli, C., Bonarini, A. & Matteucci, M. (2005) Robust detection of 3D scene horizontal and vertical lines in conical catadioptric sensors. Proceedings of the 6th Workshop on Omnidirectional Vision, Camera Networks and Non-classical cameras (OMNIVIS 2005).
22. Pratt, W.K. (2007) *Digital Image Processing*, Wiley-Interscience.
23. Scaramuzza, D. (2011) Omnidirectional camera calibration toolbox for Matlab. Available at <https://sites.google.com/site/scarabotix/ocamcalib-toolbox>.
24. Struik, D.J. (1961) *Lectures on Classical Differential Geometry*, Addison Wesley.
25. Torii, A. & Imiya, A. (2007) The randomized Hough transform based method for great circle detection on a sphere. *Pattern Recognition Letters*, issue 10, vol. 28, pp. 1186-1192.
26. Vasseur, P. & Mouaddib, E.M. (2004) Central catadioptric line detection. *Proc. 15th British Machine Vision Conf.*, Kingston University, London, pp. 57-66.
27. Ying, X. & Hu, Z. (2004) Catadioptric line features detection using hough transform. *Proc. 17th Int. Conf. on Pattern Recognition, ICPR 2004*, vol. 4, pp. 839-842.